Enhanced chemical weathering triggered an expansion of euxinic seawater in the aftermath of the Sturtian glaciation

Guang-Yi Wei[a,b*], Wei Wei[c], Dan Wang[d], Tao Li[e], Xiaoping Yang[a], Graham A. Shields[f], Feifei Zhang[a], Gaojun Li[e], Tianyu Chen[a], Tao Yang[a], Hong-Fei Ling[a]

[a]*School of Earth Sciences and Engineering, Nanjing University, 163 Xianlin Avenue, Nanjing 210023, China*

[b]*Department of Geology and Geophysics, Yale University, New Haven, CT 06520, USA*

[c]*CAS Key Laboratory of Crust-Mantle Materials and Environments, School of Earth and Space Sciences, University of Science and Technology of China, Hefei 230026, China*

[d]*School of Geographic Science, Nantong University, Nantong 226019, China*

[e]*MOE Key Laboratory of Surficial Geochemistry, Department of Earth and Planetary Sciences, Nanjing University, Nanjing 210023, China*

[f]*Department of Earth Sciences, University College London, Gower Street, London WC1E 6BT, U.K.*

*Corresponding authors: Guang-Yi Wei (guangyiwei@nju.edu.cn; wgynjues@gmail.com)

Abstract

The Cryogenian Period comprised two episodes of global glaciation (Sturtian and Marinoan glaciations) separated by a non-glacial interval, which was characterized by early radiations of eukaryotic algae and putative metazoans. Geochemical data indicate that the non-glacial interval may be marked by a transient marine oxygenation, nevertheless oceanic redox conditions varied both in time and space. Further, the links between non-glacial climate and marine redox variations are not well constrained. Here we present high-resolution lithium isotope (δ^7Li), Fe speciation and trace element (Mo and U) data for clastic sedimentary rocks from the Cryogenian interglacial Datangpo Formation, South China, in order to track the evolution of continental chemical silicate weathering and driving factors behind marine redox variability during the Cryogenian non-glacial interval. A significantly negative δ^7Li excursion of ~ -5‰ is observed in the basal Datangpo Formation, suggesting a dramatic increase in chemical silicate weathering intensity in the aftermath of the Sturtian glaciation. Expansion and contraction of anoxic-sulfidic conditions, as demonstrated by Fe speciation and trace element (Mo and U) data, mirror changes in silicate weathering intensity. Our study provides evidence that greater nutrient and sulfate availability, due to high silicate weathering intensity associated with increased exposure of fresh rocks and a warm climate, facilitated the spread of euxinic waters over the continental margins of the otherwise ferruginous Cryogenian ocean.

Keywords

Cryogenian ocean; lithium isotopes; silicate weathering; marine redox states; South China

1. Introduction

The Cryogenian Period (ca. 720–635 Ma), bookended by two global glaciations (Sturtian and Marinoan), is proposed to encompass the evolutionary origins of the earliest animals (Love et al., 2009; Burzynski et al., 2020) and the rise to dominance of eukaryotic algae (Brocks et al., 2017), both of which could be linked to secular changes in marine redox conditions. Previous studies suggested spatial heterogeneities of redox conditions at ocean margins during the Cryogenian non-glacial interval (Shields et al., 1998; Li et al., 2012) and a temporally dynamic redox state for the generally anoxic, pre-Ediacaran ocean (Zhang et al., 2015; Wei et al., 2016; Lau et al., 2017; Cheng et al., 2018). Although the first emergence of metazoans may be closely linked to changes in the Earth's surface environment, any relationship between oceanic redox condition and metazoan evolution during the Cryogenian Period is still disputed (e.g., Lau et al., 2017; Cheng et al., 2018). Furthermore, the controlling mechanisms behind secular variations in redox conditions over the continental margins are uncertain due to the lack of high-resolution geochemical records. Given that marine oxygen levels are predominately regulated by O_2 production via photosynthesis and O_2 consumption by reductants, delivery and recycling of nutrients and other redox-sensitive materials can strongly influence marine redox states. In view of this, continental weathering may have played a critical role in shaping oceanic redox landscapes in the Cryogenian non-glacial interval.

In this study, we reconstruct temporal changes in continental chemical weathering using new high-resolution lithium (Li) isotope data for the Cryogenian interglacial Datangpo Formation, South China. By comparing Li isotope data with Fe speciation data and other redox-sensitive elemental proxies (Mo, U) for local seawater redox conditions, we aim to further unravel the links between continental weathering and redox states of the Yangtze marginal sea during the Cryogenian non-glacial interval.

2. Li isotopic composition of marine detrital sediments as a proxy for continental chemical weathering

Lithium isotopes have been widely used as a tracer for silicate weathering, because Li isotopic fractionation at the Earth's surface is dominated by silicate weathering intensity and unaffected by biological processes (Lemarchand et al., 2010; Pogge von Strandmann et al., 2016). During chemical weathering, primary mineral dissolution generates no significant Li isotopic fractionation (e.g., Verney-Carron et al., 2011; Wimpenny et al., 2015), while most of the secondary minerals (i.e., clays) consistently adsorb or incorporate ^{6}Li, resulting in a large Li isotopic fractionation during the clay formation (e.g., Rudnick et al., 2004; Wimpenny et al., 2010a, 2015). Hence, continental silicate weathering generally produces low δ^7Li values combined with high Li contents in regolith (secondary clays), and high δ^7Li values with low Li concentrations in dissolved loads (e.g., Pogge von Strandmann et al., 2006, 2010; Dellinger et al., 2015, 2017). Based on studies of modern riverine suspended and dissolved loads, Li isotopes are considered to be an indicator of silicate "weathering congruency" or silicate "weathering intensity" (the ratio of chemical silicate weathering rates to total denudation rates) (cf. Dellinger et al., 2015), controlled by the relative proportion of primary mineral dissolution (producing no significant Li isotopic fractionation) to secondary clay mineral formation (producing large Li isotopic fractionation with high δ^7Li dissolved loads and low δ^7Li weathering products). The incongruent weathering regime is weathering-limited, and leads to highly fractionated Li isotopes in the dissolved loads of rivers but no appreciable Li isotopic fractionation in the detrital components, compared to the primary bedrock (i.e., moderate silicate weathering intensity) (Dellinger et al., 2014, 2015). In contrast, the congruent weathering regime is transport-limited, and shows little Li isotopic fractionation in the dissolved loads but large fractionation in the detrital components (i.e., high silicate weathering intensity) (Dellinger et al., 2017). Additionally, concurrent intense physical erosion and sluggish chemical weathering (i.e., low silicate weathering intensity) can cause the Li isotopic compositions of the dissolved and detrital loads to approach those of the bedrock, as few chemical weathering products are generated under such conditions.

The Li isotopic composition of seawater, reported from marine biogenic or abiogenic bulk carbonate, has been widely used to monitor the continental weathering process through its effect on Li isotopes in rivers (Misra and Froelich, 2012; Pogge von Strandmann et al., 2013; Lechler et al., 2015). However, there is no unambiguous way to interpret seawater δ^7Li variations because high δ^7Li values in riverine dissolved loads from incongruent weathering generally reflect intermediate silicate weathering intensity, while low δ^7Li values can reflect either the high silicate weathering intensity of a relatively congruent weathering regime, or extremely intense physical erosion with negligible chemical weathering. As a result, no simple linear correlation can be established between riverine dissolved δ^7Li values and silicate weathering intensity, which should be carefully considered when using seawater δ^7Li as a paleo-weathering proxy (Dellinger et al., 2015). Moreover, the Li isotopic composition of seawater is significantly affected by hydrothermal processes that contribute more than half of the total Li flux to modern ocean (Misra and Froelich, 2012). By contrast, the Li isotopic composition of terrestrial detrital or clay particles has been suggested as a new potential proxy for regional silicate weathering (Dellinger et al., 2017), given that the upper continental crust (UCC) has a relatively homogeneous Li isotopic composition (+0.6‰ ± 0.6‰, 2SD) (Sauzéat et al., 2015) and so any provenance effects on the δ^7Li values of weathering products are likely weak (Bastian et al., 2015; Pogge von Strandmann et al., 2017a) or can be corrected using provenance proxies (Dellinger et al., 2017).

With varying Li contents, detrital sediments in modern rivers exhibit a negative relationship between δ^7Li values and silicate weathering intensities (cf. Dellinger et al., 2017). Fine-grained marine detrital sediments or clastic sedimentary rocks (i.e., shale, mudstone and muddy siltstone), which are dominated by detrital clay minerals and rock debris, are proposed to be reliable archives for terrestrial inputs (Weaver et al., 1989; Hillier et al., 1995). Further studies confirm that continental chemical weathering, which regulates the Li isotopic compositions of weathered and eroded products, may have exerted a first-order control on the δ^7Li values of clastic sedimentary rocks (e.g., Li et al., 2016; Dellinger et al., 2017; Pogge von Strandmann et al., 2017b). In addition, low-grade metamorphism (sub-greenschist facies) has negligible impact on δ^7Li values of detrital sediments (Qiu et al., 2009). Therefore, after fully examining the effects of marine authigenic clay and terrestrial provenance, the Li isotopic compositions of marine clastic sedimentary rocks can be used to track the continental silicate weathering intensity in the ancient time.

3. Geological setting

During break-up of the supercontinent Rodinia, the South China Block underwent extension and a rift basin developed, called the Nanhua Basin, between the Yangtze and Cathaysia blocks at ca. 820 Ma (Wang and Li, 2003). The Cryogenian sedimentary strata in the Nanhua Basin comprise two major glacially influenced diamictite intervals in Guizhou Province, South China–the Tiesi'ao and Nantuo formations, which are considered to be stratigraphic equivalents of other Sturtian and Marinoan glaciogenic units, respectively, around the world (Zhang et al., 2003; Macdonald et al., 2010). The Datangpo Formation, which conformably overlies the Tiesi'ao Formation and underlies the Nantuo Formation, has been suggested as an intervening non-glacial marine sedimentary unit in South China (e.g., Li et al., 2012; Zhang et al., 2015; Wei et al., 2018). The duration of this non-glacial interval is constrained by U-Pb zircon dating of tuffaceous beds in the basal and uppermost Datangpo Formation with ages of 658.8 ± 0.5 Ma (Zhou et al., 2019) and 654.5 ± 3.8 Ma (Zhang et al., 2008), respectively (Fig. 1).

The Datangpo Formation in the Daotuo section, northeastern Guizhou in this study (Fig. 1) has a total thickness of ca. 275 m and can be subdivided into four lithological members: Member I consists of ca. 20 m of organic-rich shales interbedded with thinly layered Mn-rich carbonates, underlain by the diamictites of the Tiesi'ao Formation; Member II consists of ca. 21-m-thick organic- and sulfide-rich black shales; Member III consists of ca. 170 m gray shales; and Member IV consists of ca. 50 m gray siltstones, overlain by the massive diamictites of the Nantuo Formation. Based on paleogeographic reconstruction of South China during the Cryogenian Period (Jiang et al., 2003), the Datangpo Formation in the Daotuo section was deposited in a continental shelf to slope transitional zone on the southern margin of the Yangtze block (Fig. 1).

4. Materials and Methods

4.1 Li isotope analyses

Samples studied herein were carefully selected to avoid burial diagenetic and hydrothermal veins. The samples were ground to 200-mesh powders, and then oven-dried at 60 °C. For trace element and isotope analyses, approximately 50 mg of sample powder was weighed and firstly leached in 0.5 M acetic acid (HAc), in order to remove carbonate-associated Li (only for those samples with high Ca contents). After such weak acid leaching, 1 mL distilled HF + 4 mL distilled HNO_3 were used to digest the silicate residue at 100 °C for 12 hours. After drying, 1 mL distilled HNO_3 and 3 mL distilled HCl were further added to fully dissolve the residual components. The solutions were dried and re-dissolved in 6 N HCl in preparation for trace element and isotope analyses.

Concentrations of Trace elements were analyzed using a Thermo Element II ICP-MS at the State Key Laboratory for Mineral Deposits Research, Nanjing University. IAPSO Standard Seawater (OSIL, UK) and BHVO-2 standard (USGS) were used to monitor the long-term machine behavior. Long-term reproducibility of the measurements was typically better than 5%. Major elements (including Si, Al, Na, K, Ca, Fe) were measured using a XRF method at ALS Laboratory Group's Mineral Division, ALS Chemex, Guangzhou, China.

An AG50W-X12 cation resin was used to purify lithium in the samples. Sample solutions were dried down and re-dissolved into 1 mL 0.2 N HCl. Lithium in each sample was eluted with 0.2 N HCl, modified after James and Palmer (2000) and Dellinger et al. (2014). By checking 1 mL of the eluted solution before and after the Li elution interval, we concluded that the Li yield after the chromatographic step is > 99%, which excludes Li isotopic fractionation on the resin. The purified sample solution was used to analyze Li isotopes using a Thermo Scientific

Finnigan Neptune plus MC-ICP-MS at the MOE Key Laboratory of Surficial Geochemistry, Nanjing University. Lithium isotopic compositions of the samples and standards were consistently measured at typical Li concentrations of 25 ppb to minimize concentration-dependent isotopic effects. The ^{7}Li signal was 0.25-0.4 V/ppb under low-resolution conditions, using an Aridus II desolvating system as well as H-sample cone and X-skimmer cone. The L-SVEC lithium isotope standard (USGS) was used to calibrate the isotopic bias during the measurements using a sample–standard bracketing (SSB) method. The overall reproducibility and accuracy of the Li procedure (sample digestion, Li separation, and Li isotope analysis) were checked by repeated measurements of IAPSO Standard Seawater (δ^7Li = 30.7‰ ±0.45‰, 2SD, n = 6) and BHVO-2 (δ^7Li = 4.39‰ ± 0.32‰, 2SD, n = 3 digestions), analytical results for which are consistent with published values (e.g., Misra and Froelich, 2012; Dellinger et al., 2014, 2015).

4.2 Fe speciation analyses

Iron (Fe) speciation analyses include total Fe content (Fe_T) and highly reactive Fe content (Fe_{HR}) of the bulk samples. Highly reactive Fe comprises pyrite (Fe_{Py}), ferric oxides (Fe_{ox}), magnetite (Fe_{mag}), Fe carbonate (Fe_{carb}). The latter three Fe species are reactive to H_2S and able to convert to pyrite (Fe_{Py}) given sufficient H_2S in the water column or pore water. Ratios of Fe_{HR}/Fe_T and Fe_{Py}/Fe_{HR}, are used to evaluate the redox states of the local bottom seawater, based on statistical analyses of modern marine sediments under different redox conditions (see a recent review paper for details, Raiswell et al., 2018).

The highly reactive Fe (Fe_{carb}, Fe_{ox}, Fe_{mag}) were measured following a sequential extraction process in Poulton and Canfield (2005). Firstly, approximately 100 mg of sample powders were reacted at 50 °C for 48 hours in a sodium acetate solution with a pH of 4.5 by addition of analytical-grade acetic acid in order to extract Fe_{carb}. The residue from the first step was then reacted at room temperature for 2 hours in a 50 g/L sodium dithionite solution with a pH of 4.8 by addition of 0.2 M sodium citrate and analytical-grade acetic acid in order to extract Fe_{ox}. Then, the residue from the second step was reacted at room temperature for 6 hours in a 0.2 M ammonium oxalate and 0.17 M oxalic acid solution with a pH of 3.2 by addition of analytical-grade ammonia water to extract Fe_{mag}. All extracts were finally diluted for analyses of Fe concentration using an ICP-OES at Nanjing University with errors within 5%.

Iron in pyrite (Fe_{Py}) was calculated stoichiometrically based on pyrite-derived sulfur content (molar Fe: S = 1:2 in the pyrite) in the sample with a Cr-reduction method (Canfield et al., 1986). 20 mL of 12 M HCl and 40 mL of 1 M chromous chloride solution were added to the sample powder under a N_2-dominated condition then heated for 2 hours. The generated H_2S was deposited as Ag_2S by bubbling through 30 mL of 3% $AgNO_3$ solution, after which Ag_2S precipitate was filtered, dried and then weighed. The yield of pyrite-derived sulfur in this procedure was better than 90% based on the repeated analyses of Chinese GBW07267 pyrite standard.

4.3 Total organic carbon (TOC) analysis

For analysis of total organic carbon, sample powders were leached in 2.5 M HCl at room temperature for 48 hours to remove inorganic carbon. The residual powder was rinsed by MQ pure water and dried at 60 °C. The residues were analyzed using a CHNO-Rapid element analysis instrument at Nanjing University with analytical errors lower than ±0.1%.

5. Results

Results of lithium isotope (δ^7Li), iron speciation and trace element (Li, Mo and U) analyses for the Datangpo samples in the Daotuo section are presented in Table S1 and Figs. 2 and 3. The lower 20 m-thick calcareous, organic-rich shales in Member I have high δ^7Li values from 2.92‰ to 3.92‰, low Li contents from 4.10 ppm to 33.00 ppm, and relatively low TOC contents from 0.12% to 2.29%. The Fe_{HR}/Fe_T ratios of samples in Member I are high, ranging from 0.43 to 0.74 while the Fe_{Py}/Fe_{HR} ratios are relatively low, ranging from 0 to 0.61. The black shales in Member II show co-varying δ^7Li values from -3.38‰ to 3.53‰ and TOC contents from 1.19% to 4.26% (Fig. 2A and B). The Fe_{HR}/Fe_T and Fe_{Py}/Fe_{HR} ratios of this member are high, ranging from 0.61 to 0.98 and from 0.76 to 0.94, respectively. The gray shales and muddy siltstones in Members III and IV uniformly have high δ^7Li values and Li contents, and low TOC contents, with average values of 1.14‰, 62.2 ppm and 0.30%, respectively. Except for four samples in the lowermost Member III, which have relatively high Fe_{HR}/Fe_T and Fe_{Py}/Fe_{HR} ratios, all the samples in Member III and IV have uniformly low Fe_{HR}/Fe_T and Fe_{Py}/Fe_{HR} ratios, ranging from 0.18 to 0.41 and from 0.12 to 0.31, respectively. All the samples in the Datangpo Formation are relatively depleted in Mo and U, except for those in the lower Member II recording a peak of Mo concentration up to 48.11 ppm.

6. Discussion

6.1 Li isotope constraints on continental chemical weathering following the Sturtian

deglaciation

Lithium concentrations and isotopic compositions of the shales and muddy siltstones from the Datangpo Formation were investigated to track the evolution of chemical weathering in the aftermath of the Sturtian glaciation. Lithium in marine fine-grained aluminosilicate rocks (i.e., shale, mudstone and muddy siltstone) is generally hosted in the terrestrial weathering products and unweathered fragments of igneous and sedimentary rocks that are transported via river to the sea (cf. Dellinger et al., 2014), as well as in authigenic clays precipitating from seawater (marine reverse weathering) (e.g., Weaver et al., 1989; Hillier et al., 1995). Thus, Li isotopes of the bulk marine clastic sedimentary rocks are controlled by the proportions of terrestrial detrital materials and marine authigenic clays, as well as their Li isotopic compositions. In order to better monitor the continental weathering process, effects of authigenic clay formation on the Li isotopic composition of bulk samples should firstly be examined, as authigenic clays generated from seawater generally have distinctively higher δ^7Li values, compared to terrestrial weathering products (Chan et al., 2002, 2006).

In this study, concentrations of Be, Sc, Ti, Th and their relationships with the Al concentration are used as indicators of the contributions from marine authigenic clays to bulk samples. Seawater generally has extremely low dissolved Be, Sc, Ti and Th concentrations as these elements are insoluble, incompatible and thus enriched in the continental crust (Whitfield and Turner, 1979; Taylor and McLennan, 1985). In this view, marine authigenic clays, which represent the aluminosilicate minerals directly precipitating from seawater, should have high Al contents but significantly low Be, Sc, Ti and Th concentrations. This hypothesis is well supported by the modern authigenic clays in the South Pacific Gyre sediments that exhibit depletion in these elements (cf. Dunlea et al., 2015). Compared to modern marine authigenic clays, the studied samples in the Datangpo Formation show much higher Be, Sc, Ti and Th concentrations and significant linear correlations of Al–Be, Al–Sc, Al–Ti and Al–Th (Fig. 4). Further, average ratios of Al/Be, Al/Sc, Al/Ti and Al/Th of the studied samples approach those of the UCC (Rudnick and Gao, 2014) (Fig. 4). All these observations suggest that the aluminosilicates in bulk samples from this study are predominantly derived from the UCC, rather than seawater. Therefore, while it may not be easy to completely exclude an influence of marine authigenic clays on the studied samples, above discussion of trace elements Be, Sc, Ti and Th can provide, in part, independent evidence that bulk shales and muddy siltstones in the Datangpo Formation are dominated by terrestrial detrital materials.

Studies of Li isotope behavior in modern riverine suspended materials concluded that the δ^7Li values of terrestrial detrital materials are potentially determined by rock provenance, grain size and silicate weathering intensity (Dellinger et al., 2014, 2017; Pogge von Strandmann et al., 2017a). The Al/Si ratio of the detrital sediments is widely used to constrain the effect of grain size on bulk δ^7Li values (Bouchez et al., 2011; Dellinger et al., 2014). Compared to modern river sands (Al/Si < 0.15, Dellinger et al., 2014), the bulk samples in this study show relatively uniform and high Al/Si ratios (0.32 on average) and no appreciable relationship between δ^7Li values and Al/Si ratios (Fig. 5A). Additionally, samples in this study exhibit variable Li/Al ratios and less variable Na/Al ratios, but exhibit no clear correlation between Li/Al and Na/Al ratios (Fig. 5B). The studied samples also have much higher Na/Al ratios but lower Li/Al ratios compared to the clastic sedimentary rock endmember defined in Dellinger et al. (2014). All these observations suggest that the elemental and isotopic differences from the studied samples were mainly due to variations in silicate weathering intensity, and not just derived from the mixing debris of igneous vs. sedimentary rocks or recycling of earlier sedimentary rocks (cf. Dellinger et al., 2014). Taken together, variations in bulk δ^7Li values of the Datangpo samples are most likely indicative of changes in silicate weathering intensity following the Sturtian deglaciation.

Datangpo Member I samples have high δ^7Li values (~ 3.53‰) (Fig. 2A), with compositions much closer to average mid-ocean ridge basalt ($\delta^7\mathrm{Li}_{\mathrm{MORB}}$ = 3.4 ± 0.7‰, Tomascak et al., 2008), instead of the UCC ($\delta^7\mathrm{Li}_{\mathrm{UCC}}$ = 0.6 ± 0.6‰, Sauzéat et al., 2015). Given a lower average Li concentration (~ 16.1 ppm) for the Member I samples relative to the UCC (~ 30.5 ppm, Sauzéat et al., 2015) and granites (~ 30.9 ppm, Bryant et al., 2004), samples with relatively high δ^7Li values in Member I more likely archive the products of physical erosion of mafic rocks in the Sturtian post-glaciation, potentially linked to the extensive emplacement of large basaltic igneous provinces following the Rodinia break-up (Gernon et al., 2016; Cox et al., 2016). Lithium concentrations and δ^7Li values recorded in the Datangpo Member I highlight high physical erosion and low silicate weathering intensity immediately following the deglaciation, and are consistent with Li isotope records for modern glaciated basaltic terrains (Pogge von Strandmann et al., 2006, 2010; Wimpenny et al., 2010b; Millot et al., 2010). By contrast, black shales in Member II are marked by a dramatic negative δ^7Li excursion with δ^7Li values as low as –3.38‰, and relatively high Li concentrations (~ 26.5 ppm). Although continental weathering processes do not simply determine Li contents of the detrital sediments, fine-grained sediments from modern lowland terrains with high silicate weathering intensity may have appreciably low Li concentrations (Dellinger et al., 2017). Compared to the UCC ($\delta^7\mathrm{Li}_{\mathrm{UCC}}$

= 0.6 ± 0.6‰, $[Li]_{UCC}$ = 30.5 ± 3.6 ppm), notably low δ^7Li values as well as relatively lower Li concentrations of the Member II black shales suggest more congruent chemical weathering regime in this interval, which means less uptake of Li into secondary clays relative to Li release from the bed rocks (Dellinger et al., 2014, 2017; Dosseto et al., 2015). This congruent chemical weathering is considered as a transport-limited condition, analogous to the chemical weathering regime in modern Amazon lowlands, implying high silicate weathering intensity during early stages of the Cryogenian non-glacial interval. Black shales in the uppermost parts of Member II record a gradual increase in δ^7Li values, indicative of weakening silicate weathering intensity. Gray shales and siltstones of members III and IV show consistently high δ^7Li values (~ 1.1‰), close to the δ^7Li value of the UCC (0.6 ± 0.6‰). Considering that Li concentrations of the gray shales and siltstones (~ 62.2 ppm) are much higher than that of the UCC (30.5 ± 3.6 ppm), high δ^7Li values of these samples are more likely caused by an incongruent chemical weathering regime, during which Li is quantitatively incorporated into secondary clays and then transported to continental margins with a moderate silicate weathering intensity (cf. Dellinger et al., 2017).

Given that the Li isotopic compositions of bulk samples from the Datangpo Formation are linked to changes in continental physical erosion and chemical weathering, correlations between δ^7Li values, Li concentrations and Li/Al ratios are further investigated to track the effects of rock provenance, physical erosion and chemical weathering on Li isotopic compositions of terrestrial detrital sediments (e.g., Millot et al., 2010; Dellinger et al., 2014). Three endmembers of detrital materials produced under different silicate weathering intensities (Fig. 6A and B) are defined here (A): product of physical erosion in the glaciated basaltic terrain (data modified from Pogge von Strandmann et al., 2006, 2010; Wimpenny et al., 2010b); endmember (B) product of congruent chemical weathering (high silicate weathering intensity, corresponding to modern Amazon and Congo rivers) (data from Dellinger et al., 2014, 2017 and references therein); and endmember (C) product of incongruent chemical weathering (low silicate weathering intensity) based on modern riverine suspended materials (data from Dellinger et al., 2014, 2017 and references therein). Samples of the Datangpo Formation in this study exhibit clear covariation between Li concentrations or Li/Al ratios and δ^7Li values (Fig. 6), representing the evolution of two continental weathering regimes (A–B and A–C trends) in the Cryogenian non-glacial interval. Analogous to modern lowlands of the Amazon and Congo rivers, the significant negative δ^7Li excursion observed in the Datangpo Member II (Fig. 2) suggests a gradually enhanced silicate weathering intensity, approaching highly congruent weathering conditions in the aftermath of the Sturtian glaciation (trend A–B in Fig. 6). This is consistent with the suggestion of intense silicate weathering during the early stage of deglaciation caused by warm climate and the exposure of fresh mineral surfaces via glacial erosion (Prestrud Anderson et al., 1997; Mills et al., 2011; Fabre and Berger, 2012). Following the negative excursion, δ^7Li values rapidly increase in the middle and upper Datangpo Formation and approach that of average UCC (Fig. 2). Higher δ^7Li values in Member III and IV suggest an incongruent weathering condition (moderate silicate weathering intensity), which is analogous to modern regions with relatively weak silicate weathering (trend A–C in Fig. 6). The changes in silicate weathering intensity from the middle to upper Datangpo Formation might reflect the initiation of global cooling before the Marinoan glaciation.

6.2 Evolution of marine redox states in the Yangtze margin area following the Sturtian

deglaciation

Redox states of the Cryogenian non-glacial ocean have been investigated in previous studies based on analyses of various proxies. Uranium isotopes of shallow carbonates in Mongolia suggested a transient oceanic oxygenation in the aftermath of the Sturtian glaciation and subsequent expansion of marine anoxia (Lau et al., 2017). Molybdenum isotopes of black shales in South China imply that the global sub-surface ocean was largely anoxic during the Cryogenian non-glacial interval (Cheng et al., 2018). Additionally, iron speciation analyses of the black shales in South China suggest a highly stratified seawater structure with extensive anoxic deep waters in the Yangtze marginal area, which is also evidenced by variable and extremely high $\delta^{34}S$ in pyrites and high $\delta^{15}N$ in black shales during this period (e.g., Li et al., 2012; Wei et al., 2016). To better constrain the links between chemical weathering and redox state of continental shelf seawater during the Cryogenian non-glacial interval, iron speciation and redox-sensitive trace elements (Mo and U) were also analyzed for the samples in this study.

6.2.1 Fe speciation

Based on Fe speciation framework for modern marine sediments under different local redox conditions, samples with Fe_{HR}/Fe_T exceeding 0.38 are generally deposited beneath anoxic bottom waters. The threshold value can be reduced to 0.22 due to thermal alteration of ancient rocks (see Raiswell et al., 2018 for a detailed review). Further, available Fe_{HR} tends to be converted to Fe_{Py} where free H_2S has accumulated in anoxic seawater via microbial sulfate reduction, thus samples with $Fe_{HR}/Fe_T > 0.38$ and $Fe_{Py}/Fe_{HR} > 0.7–0.8$ are considered to precipitate from the euxinic (sulfidic) bottom waters (Raiswell et al., 2018). Additionally, low Fe_{HR}/Fe_T (0.2–0.3) and high Fe_{Py}/Fe_{HR} (> 0.9) are considered to reflect relatively high H_2S

concentration in sediment pore water, rather than bottom water-mass (Hardisty et al., 2018).

The samples from the Datangpo Formation have consistently higher total Fe concentration (average Fe_T = 4%) and Fe/Al ratio (average $Fe_T/Al = 0.46$), relative to the UCC (Fe_T = 3.5%, $Fe_T/Al = 0.44$; Rudnick and Gao, 2014). An absence of covariation between Fe_T and Al concentrations indicate that changes in Fe_T concentration are not controlled by terrestrial detrital input. Thus, iron speciation data in this study can be taken to reflect redox conditions of local bottom waters (cf. Clarkson et al., 2014; Scholz et al., 2019). As shown in Fig. 3D and E, the Fe_{HR}/Fe_T ratios of the samples in Datangpo members I and II are higher than 0.38, suggesting that anoxic bottom waters dominated in the Yangtze marginal area at the start of the non-glacial period. In contrast, samples from members III and IV (except for the lowest three samples), whose Fe_{HR}/Fe_T ratios are mostly lower than 0.38, were more likely deposited in an oxic marine environment. Further, Fe_{Py}/Fe_{HR} ratios in Datangpo Member II are mostly higher than 0.7–0.8, and so bolster the view that the black shale unit (Member II) of the Datangpo Formation was deposited under predominantly euxinic conditions (Li et al., 2012; Cheng et al., 2018).

6.2.2 Mo- and U-enrichment patterns

Black shales in Datangpo Member II show a peak of Mo enrichment (up to 48.1 ppm), consistent with significant Mo enrichment in euxinic sediments. Whereas, U in the entire Datangpo Formation is not appreciably enriched ($U_{average}$ = 2.76 ppm), compared with the UCC (U_{UCC} = 2.7 ppm, Rudnick and Gao, 2014). Studies of modern reducing sediments have built a framework to interpret local marine depositional conditions using Mo–TOC and Mo_{EF}–U_{EF}

covariations (Algeo and Lyons, 2006; Algeo and Tribovillard, 2009). The relationship between Mo and TOC in reducing sediments has been used to constrain the degree of basin restriction based on the case that rapid Mo precipitation induces significant Mo depletion in the local water column and thus low Mo/TOC ratios of sediments in a strongly restricted basin without sufficient replenishment of Mo from the open ocean (Algeo and Lyons, 2006). Therefore, Mo/TOC ratios of modern reducing sediments (the dashed lines in Fig. 7C) show a gradually decreasing trend accompanying enhanced basin restriction. In addition, because of the different geochemical behaviors of Mo and U under anoxic and euxinic conditions, Mo_{EF} vs. U_{EF} [enrichment factors of Mo and U defined by element $X_{EF} = (X/Al)_{sample} / (X/Al)_{PAAS}$] covariation in reducing sediments is widely used to track the local depositional environment as well as basin restriction (arrows in Fig. 7D) (Algeo and Tribovillard, 2009; Tribovillard et al., 2012). Given the robust constraints on redox conditions of bottom water from Fe speciation data, global Mo–U cycling through the Cryogenian non-glacial interval is further unraveled by using Mo–TOC and Mo_{EF}–U_{EF} covariations of samples from the Datangpo Formation.

In this study, appreciable Mo enrichments can be observed in the Datangpo Member I and II (Mo_{EF} up to ~ 60), whereas U is depleted throughout the entire Datangpo Formation (U_{EF} = ~ 1). The Mo/TOC ratios of the Datangpo samples are generally lower than those of sediments in the modern Black Sea (Fig. 7C), which were previously interpreted to be a result of the strongly restricted depositional environment of the Nanhua Basin (e.g., Li et al., 2012). However, the Mo_{EF}/U_{EF} ratios of most samples in this study are much higher than that of modern seawater (Fig. 7D), which is quite different from the situation for the modern strongly restricted basin (e.g., Black Sea). Combined with Fe speciation data from the Datangpo samples constraining local marine redox states in Yangtze marginal seawater, systemic analysis of Mo–U covariations can provide more insights into global oceanic redox evolution, by considering secular changes in global Mo and U ocean reservoirs (cf. Scott et al., 2008; Partin et al., 2013). Different from the Mo–TOC and Mo_{EF}–U_{EF} pattern of modern reducing sediments, which are deposited beneath waterbodies with high Mo and U concentrations, the mostly low Mo/TOC and high Mo_{EF}/U_{EF} ratios of the Datangpo samples are more likely indicative of moderately low Mo and extremely low U concentrations in seawater, corresponding to much smaller Mo and U reservoirs in the Cryogenian global ocean, compared to the modern ocean (cf. Scott et al., 2008; Partin et al., 2013; Reinhard et al., 2013). The decoupled records of Mo and U concentrations of the black shales in the lower Datangpo Formation and the steep slope with low U_{EF} (~ 1) of the samples plotted on the Mo_{EF}-U_{EF} diagram (Fig. 7D) suggest that the marine U reservoir may have been significantly smaller than the Mo reservoir in the Cryogenian ocean, likely due to more scavenging of U relative to Mo from anoxic and non-euxinic seawater. This scenario is supported by the case that the early Neoproterozoic ocean was characterized by predominantly ferruginous rather than sulfidic conditions (e.g., Guilbaud et al., 2015). Hence, Fe speciation and Mo–U enrichments in the Datangpo Formation, South China are indicative of an episodic but widespread expansion of euxinic seawater over the continental margin during the Cryogenian non-glacial interval.

6.3 Possible links between continental chemical weathering and redox state of continental margin ocean

Studies of the Datangpo Formation, South China suggested a dynamic redox landscape for Yangtze marginal seawater with extensive marine euxinia following Sturtian deglaciation (Li et al., 2012; Cheng et al., 2018; this study). Dynamically changing redox states after the Sturtian glaciation reflect transitions between euxinic and ferruginous conditions on the Yangtze margin, likely driven by continental chemical weathering. Previous studies have suggested widespread ferruginous conditions and only spatially limited euxinic conditions during the middle Proterozoic (Planavsky et al., 2011; Gilleaudeau et al., 2019), during which continental chemical weathering and marine primary productivity were significantly depressed (Crockford et al., 2018; Rafiei et al., 2019). In this view, transitions of local marine ferruginous and euxinic conditions in the aftermath of the Sturtian glaciation were more likely controlled by microbially mediated sulfate reduction linked to changes in continental weathering and marine primary productivity(e.g., Reinhard et al., 2009; Planavsky et al., 2011; Li et al., 2012; Guilbaud et al., 2015).

In the context of significant correlations between Fe_{HR}/Fe_T, Fe_{Py}/Fe_{HR} and δ^7Li values (Fig. 8), the expansion of marine euxinia in the Yangtze marginal area could be attributed to a significant increase in silicate weathering intensity, characterized by consistently high Fe_{HR}/Fe_T and Fe_{Py}/Fe_{HR} ratios, and low δ^7Li values in the Datangpo Member II (Fig. 8). During the Sturtian glaciation, as most of the continents were fully covered by ice, chemical weathering of terrestrial materials, including pyrite, might have almost ceased, resulting in extremely low oceanic sulfate concentration and thus only ferruginous conditions in the deep marine realm without much euxinic seawater (i.e., sulfate-limited condition). Based on Li isotope data in this study, Datangpo Member I was deposited when continental margin sea ice had disappeared and physical erosion of continental mafic igneous rocks could dominate the terrestrial inputs to the ocean (Fig. 9A). Thus, this interval inherited low oceanic sulfate and Mo concentrations from the glacial period.

Given that more continental fresh rock surfaces were exposed to chemical weathering after the long-term glacial erosion (Prestrud Anderson et al., 1997; Mills et al., 2011; Fabre and Berger, 2012), high silicate weathering intensity during the Datangpo Member II interval likely triggered a concurrent increase in silicate weathering flux prior to the development of deep soils (Fig. 9B). The consistently enhanced silicate weathering intensity and flux could effectively elevate nutrient (e.g., P) fluxes delivered to the continental margin ocean in the early deglacial period (cf. Hawkings et al., 2016; Li et al., 2018). Likewise, coupled increase in weathering intensity and availability after such long-term glacial erosion, could also facilitate the release of sulfate and Mo in early stages of deglaciation, by promoting the oxidative weathering of sulfide minerals (e.g., Sahoo et al., 2012; Torres et al., 2017). The fertilization of Yangtze marginal seawater due to the high silicate weathering intensity and flux may have consequently promoted primary productivity and microbial sulfate reduction in the aftermath of the Sturtian glaciation, recorded by high TOC and Fe_{Py}/Fe_{HR} in the Datangpo Member II samples (Fig. 9B). The expansion of marine euxinia as well as increased import of Mo to the continental margin ocean induced rapid Mo accumulation in the lower Datangpo Member II. Seawater U concentrations might have increased slightly but were still low as indicated by notably low U contents of the Member II samples (Fig. 3B), as marine U reservoir was much smaller than the Mo reservoir in the Cryogenian ocean. Additionally, increased silicate weathering intensity might have led to the development of deep soils under a relatively quiescent tectonic regime. As shown in modern lowlands of Amazon and Congo rivers, the exhaustion of fresh rocks, followed by formation of deep soils, could subsequently decrease the weathering flux (cf.

Dellinger et al., 2015). By analogy, this waning in silicate weathering flux would inhibit the further delivery of nutrients to continental margin ocean and reduced primary productivity in later post-glacial stages, which corresponds to the rapid decline in the TOC of the upper Member II (Fig. 2B). Compared to silicate weathering, the decline in oxidative weathering flux of sulfides (i.e., release of sulfate and Mo) is more rapid, due to the easier exhaustion of fresh sulfides than silicate minerals during early post-glacial stages (cf. Torres et al., 2017). Thus, together with decline in terrestrial Mo supply, scavenging of Mo in the euxinic seawater resulted in a sharp decrease in Mo concentrations of the upper Datangpo Member II (Fig. 3A), even though euxinic conditions still dominated this interval (Fig. 3E).

High δ^7Li and low TOC of the Datangpo Member III and IV samples indicate that the middle to late Cryogenian non-glacial interval experienced low silicate weathering intensity and potentially low primary productivity (Fig. 2A and B), which was likely linked to a transition from relatively warm climate to cooler climate under conditions of relatively high tectonic stability (i.e., Marinoan glaciation). The waning of euxinic seawater may have been related to more limited sulfate supply and lower organic production in the oceans due to suppressed continental silicate weathering intensity and availability.

7. Conclusions

New high-resolution δ^7Li data from the Datangpo Formation, South China are used to track temporal variations in continental silicate weathering intensity during the Cryogenian non-glacial interval. A significantly negative δ^7Li excursion in the basal Datangpo Formation was caused by enhanced silicate weathering intensity in the aftermath of the Sturtian glaciation. By contrast, high δ^7Li values in the lowest, middle and upper Datangpo Formation suggest relatively low silicate weathering intensity in the earliest and later parts of the non-glacial interval. Coupled increase in continental silicate weathering intensity and land surface reactivity coincided with the expansion of euxinic seawater in the Yangtze marginal area in the aftermath of the Sturtian glaciation. Large inputs of nutrients and sulfate due to high continental silicate weathering intensity and flux would have intensified marine primary productivity and stimulated microbial sulfate reduction on continental margins. The transient spread of marine euxinia was therefore driven by enhanced continental weathering following the Sturtian deglaciation.

Acknowledgements

This study was funded by the Strategic Priority Research Program (B) of the Chinese Academy of Sciences (CAS) (XDB26000000) and the National Natural Science Foundation of China (NSFC) program [41872002, 41661134048 (BETR)]. Guang-Yi Wei acknowledges the support from the program A for Outstanding PhD. Candidate of Nanjing University (No.201802A020). Wei Wei acknowledges the funding from NSFC program 41902025. Dan Wang acknowledges the funding from NSFC program 41603023. We thank Prof. Noah Planavsky for assistance with the lab work and useful discussion. We also thank Editor Itay Halevy for handling this paper; Prof. Paul Tomascak and an anonymous reviewer for constructive reviews that greatly improved this paper.

References

Algeo, T.J., Lyons, T.W., 2006. Mo-total organic carbon covariation in modern anoxic marine environments: Implications for analysis of paleoredox and paleohydrographic conditions. Paleoceanography 21, PA1016.

Algeo, T.J., Tribovillard, N., 2009. Environmental analysis of paleoceanographic systems based on molybdenum–uranium covariation. Chemical Geology 268, 211-225.

Bastian, L., Revel, M., Vigier, N., 2015. Investigating Li Isotope Composition of Nile Deltaic Sediments as Paleotracer of Continental Alteration. Procedia Earth and Planetary Science 13, 261-264.

Bouchez, J., Gaillardet, J., France-Lanord, C., Maurice, L., Dutra-Maia, P., 2011. Grain size control of river suspended sediment geochemistry: Clues from Amazon River depth profiles. Geochemistry, Geophysics, Geosystems 12, Q03008.

Brocks, J.J., Jarrett, A.J.M., Sirantoine, E., Hallmann, C., Hoshino, Y., Liyanage, T., 2017. The rise of algae in Cryogenian oceans and the emergence of animals. Nature 548, 578-581.

Bryant, C.J., Chappell, B.W., Bennett, V.C., McCulloch, M.T., 2004. Lithium isotopic compositions of the New England Batholith: correlations with inferred source rock compositions. Earth and Environmental Science Transactions of the Royal Society of Edinburgh 95, 199-214.

Burzynski, G., Dececchi, T.A., Narbonne, G.M., Dalrymple, R.W., 2020. Cryogenian Aspidella from northwestern Canada. Precambrian Research 336, 105507.

Canfield, D.E., Raiswell, R., Westrich, J.T., Reaves, C.M., Berner, R.A., 1986. The use of chromium reduction in the analysis of reduced inorganic sulfur in sediments and shales. Chemical Geology 54, 149-155.

Chan, L.-H., Alt, J.C., Teagle, D.A.H., 2002. Lithium and lithium isotope profiles through the upper oceanic crust: a study of seawater–basalt exchange at ODP Sites 504B and 896A. Earth and Planetary Science Letters 201, 187-201.

Chan, L.-H., Leeman, W.P., Plank, T., 2006. Lithium isotopic composition of marine sediments. Geochemistry, Geophysics, Geosystems 7, Q06005.

Cheng, M., Li, C., Chen, X., Zhou, L., Algeo, T.J., Ling, H.-F., Feng, L.-J., Jin, C.-S., 2018. Delayed Neoproterozoic oceanic oxygenation: Evidence from Mo isotopes of the Cryogenian Datangpo Formation. Precambrian Research 319, 187-197.

Clarkson, M. O., Poulton, S. W., Guilbaud, R. and Wood, R. A., 2014. Assessing the utility of Fe/Al and Fe-speciation to record water column redox conditions in carbonate-rich sediments. Chemical Geology 382, 111-122.

Cox, G.M., Halverson, G.P., Stevenson, R.K., Vokaty, M., Poirier, A., Kunzmann, M., Li, Z.-X., Denyszyn, S.W., Strauss, J.V., Macdonald, F.A., 2016. Continental flood basalt weathering as a trigger for Neoproterozoic Snowball Earth. Earth and Planetary Science Letters 446, 89-99.

Crockford, P. W., Hayles, J. A., Bao, H., Planavsky, N. J., Bekker, A., Fralick, P. W., Halverson, G. P., Bui, T. H., Peng, Y. and Wing, B. A., 2018. Triple oxygen isotope evidence for limited mid-Proterozoic primary productivity. Nature 559, 613-616.

Dellinger, M., Bouchez, J., Gaillardet, J., Faure, L., Moureau, J., 2017. Tracing weathering regimes using the lithium isotope composition of detrital sediments. Geology 45, 411-414.

Dellinger, M., Gaillardet, J., Bouchez, J., Calmels, D., Galy, V., Hilton, R.G., Louvat, P., France-Lanord, C., 2014. Lithium isotopes in large rivers reveal the cannibalistic nature of modern continental weathering and erosion. Earth and Planetary Science Letters 401, 359-372.

Dellinger, M., Gaillardet, J., Bouchez, J., Calmels, D., Louvat, P., Dosseto, A., Gorge, C., Alanoca, L., Maurice, L., 2015. Riverine Li isotope fractionation in the Amazon River basin controlled by the weathering regimes. Geochimica et Cosmochimica Acta 164, 71-93.

Dosseto, A., Vigier, N., Joannes-Boyau, R., Moffat, I., Singh, T., Srivastava, P., 2015. Rapid response of silicate weathering rates to climate change in the Himalaya. Geochemical Perspectives Letters 1, 10-19.

Dunlea, A.G., Murray, R.W., Sauvage, J., Spivack, A.J., Harris, R.N., D'Hondt, S., 2015. Dust, volcanic ash, and the evolution of the South Pacific Gyre through the Cenozoic. Paleoceanography 30, 1078-1099.

Fabre, S., Berger, G., 2012. How tillite weathering during the snowball Earth aftermath induced cap carbonate deposition. Geology 40, 1027-1030.

Gernon, T.M., Hincks, T.K., Tyrrell, T., Rohling, E.J., Palmer, M.R., 2016. Snowball Earth ocean chemistry driven by extensive ridge volcanism during Rodinia breakup. Nature Geoscience 9, 242-248.

Gilleaudeau, G. J., Romaniello, S. J., Luo, G., Kaufman, A. J., Zhang, F., Klaebe, R. M., Kah, L. C., Azmy, K., Bartley, J. K., Zheng, W., Knoll, A. H. and Anbar, A. D., 2019. Uranium isotope evidence for limited euxinia in mid-Proterozoic oceans. Earth and Planetary Science Letters 521, 150-157.

Guilbaud, R., Poulton, S. W., Butterfield, N. J., Zhu, M. and Shields-Zhou, G. A., 2015. A global transition to ferruginous conditions in the early Neoproterozoic oceans. Nature Geoscience 8, 466-470.

Hardisty, D. S., Lyons, T. W., Riedinger, N., Isson, T. T., Owens, J. D., Aller, R. C., Rye, D. M., Planavsky, N. J., Reinhard, C. T., Gill, B. C., Masterson, A. L., Asael, D. and Johnston, D. T., 2018. An evaluation of sedimentary molybdenum and iron as proxies for pore fluid paleoredox conditions. American Journal of Science 318, 527-556.

Hawkings, J., Wadham, J., Tranter, M., Telling, J., Bagshaw, E., Beaton, A., Simmons, S.-L., Chandler, D., Tedstone, A. and Nienow, P., 2016. The Greenland Ice Sheet as a hot spot of phosphorus weathering and export in the Arctic. Global Biogeochemical Cycles 30, 191-210.

Hillier, S., 1995. Erosion Sedimentation and Sedimentary Origin of Clays. Origin and mineralogy of clays. Springer, Berlin.

James, R.H., Palmer, M. R., 2000. The lithium isotope composition of international rock standards. Chemical Geology 166, 319-326.

Jiang, G., Sohl, L., Christie-Blick, N., 2003. Neoproterozoic stratigraphic comparison of the Lesser Himalaya (India) and Yangtze block (south China): Paleogeographic implications. Geology 31, 917-920.

Lau, K.V., Macdonald, F.A., Maher, K., Payne, J.L., 2017. Uranium isotope evidence for temporary ocean oxygenation in the aftermath of the Sturtian Snowball Earth. Earth and Planetary Science Letters 458, 282-292.

Lemarchand, E., Chabaux, F., Vigier, N., Millot, R., Pierret, M.-C., 2010. Lithium isotope systematics in a forested granitic catchment (Strengbach, Vosges Mountains, France).

Geochimica et Cosmochimica Acta 74, 4612-4628.

Lechler, M., Pogge von Strandmann, P.A.E., Jenkyns, H.C., Prosser, G., Parente, M., 2015. Lithium-isotope evidence for enhanced silicate weathering during OAE 1a (Early Aptian Selli event). Earth and Planetary Science Letters 432, 210-222.

Li, C., Cheng, M., Zhu, M. and Lyons, T. W., 2018. Heterogeneous and dynamic marine shelf oxygenation and coupled early animal evolution. Emerging Topics in Life Sciences 2, 279-288.

Li, C., Love, G.D., Lyons, T.W., Scott, C.T., Feng, L., Huang, J., Chang, H., Zhang, Q., Chu, X., 2012. Evidence for a redox stratified Cryogenian marine basin, Datangpo Formation, South China. Earth and Planetary Science Letters 331-332, 246-256.

Li, S., Gaschnig, R.M., Rudnick, R.L., 2016. Insights into chemical weathering of the upper continental crust from the geochemistry of ancient glacial diamictites. Geochimica et Cosmochimica Acta 176, 96-117.

Love, G.D., Grosjean, E., Stalvies, C., Fike, D.A., Grotzinger, J.P., Bradley, A.S., Kelly, A.E., Bhatia, M., Meredith, W., Snape, C.E., Bowring, S.A., Condon, D.J., Summons, R.E., 2009. Fossil steroids record the appearance of Demospongiae during the Cryogenian period. Nature 457, 718-721.

Macdonald, F.A., Schmitz, M.D., Crowley, J.L., Roots, C.F., Jones, D.S., Maloof, A.C., Strauss, J.V., Cohen, P.A., Johnston, D.T., Schrag, D.P., 2010. Calibrating the Cryogenian. Science 327, 1241-1243.

Millot, R., Vigier, N., Gaillardet, J., 2010. Behaviour of lithium and its isotopes during weathering in the Mackenzie Basin, Canada. Geochimica et Cosmochimica Acta 74, 3897-

3912.

Mills, B., Watson, A.J., Goldblatt, C., Boyle, R., Lenton, T.M., 2011. Timing of Neoproterozoic glaciations linked to transport-limited global weathering. Nature Geoscience 4, 861-864.

Misra, S., Froelich, P. N., 2012. Lithium isotope History of Cenozoic Seawater: Changes in Silicate Weathering and Reverse Weathering. Science 335, 818-823.

Partin, C. A., Bekker, A., Planavsky, N. J., Scott, C. T., Gill, B. C., Li, C., Podkovyrov, V., Maslov, A., Konhauser, K. O., Lalonde, S. V., Love, G. D., Poulton, S. W. and Lyons, T. W., 2013. Large-scale fluctuations in Precambrian atmospheric and oceanic oxygen levels from the record of U in shales. Earth and Planetary Science Letters 369-370, 284-293.

Planavsky, N. J., McGoldrick, P., Scott, C. T., Li, C., Reinhard, C. T., Kelly, A. E., Chu, X., Bekker, A., Love, G. D. and Lyons, T. W., 2011. Widespread iron-rich conditions in the mid-Proterozoic ocean. Nature 477, 448-451.

Pogge von Strandmann, P.A.E., Burton, K.W., James, R.H., van Calsteren, P., Gislason, S.R., 2010. Assessing the role of climate on uranium and lithium isotope behaviour in rivers draining a basaltic terrain. Chemical Geology 270, 227-239.

Pogge von Strandmann, P.A.E., Burton, K.W., James, R.H., van Calsteren, P., Gíslason, S.R., Mokadem, F., 2006. Riverine behaviour of uranium and lithium isotopes in an actively glaciated basaltic terrain. Earth and Planetary Science Letters 251, 134-147.

Pogge von Strandmann, P.A.E., Burton, K.W., Opfergelt, S., Eiríksdóttir, E.S., Murphy, M.J., Einarsson, A., Gislason, S.R., 2016. The effect of hydrothermal spring weathering processes and primary productivity on lithium isotopes: Lake Myvatn, Iceland. Chemical Geology 445, 4-13.

Pogge von Strandmann, P.A.E., Frings, P.J., Murphy, M.J., 2017a. Lithium isotope behaviour during weathering in the Ganges Alluvial Plain. Geochimica et Cosmochimica Acta 198, 17-31.

Pogge von Strandmann, P.A.E., Desrochers, A., Murphy, M.J., Finlay, A.J., Selby, D., Lenton, T.M., 2017b. Global climate stabilisation by chemical weathering during the Hirnantian glaciation. Geochemical Perspectives Letters 3, 230-237.

Pogge von Strandmann, P.A.E., Jenkyns, H.C., Woodfine, R.G., 2013. Lithium isotope evidence for enhanced weathering during Oceanic Anoxic Event 2. Nature Geoscience 6, 668-672.

Poulton, S., Canfield, D., 2005. Development of a sequential extraction procedure for iron: implications for iron partitioning in continentally derived particulates. Chemical Geology 214, 209-221.

Prestrud Anderson, S., Drever, J. I., Humphrey, N. F., 1997. Chemical weathering in glacial environment. Geology 25, 399-402.

Qiu, L., Rudnick, R.L., McDonough, W.F., Merriman, R.J., 2009. Li and δ^7Li in mudrocks from the British Caledonides: Metamorphism and source influences. Geochimica et Cosmochimica Acta 73, 7325-7340.

Rafiei, M. and Kennedy, M., 2019. Weathering in a world without terrestrial life recorded in the Mesoproterozoic Velkerri Formation. Nat Commun 10, 3448.

Raiswell, R., Hardisty, D.S., Lyons, T.W., Canfield, D.E., Owens, J.D., Planavsky, N.J., Poulton, S.W., Reinhard, C.T., 2018. The iron paleoredox proxies: A guide to the pitfalls, problems and proper practice. American Journal of Science 318, 491-526.

Reinhard, C. T., Planavsky, N. J., Robbins, L. J., Partin, C. A., Gill, B. C., Lalonde, S. V., Bekker, A., Konhauser, K. O. and Lyons, T. W., 2013. Proterozoic ocean redox and biogeochemical stasis. Proc. Natl. Acad. Sci. USA 110, 5357-5362.

Reinhard, C. T., Raiswell, R., Scott, C., Anbar, A. D., Lyons, T. W., 2009. A Late Archean Sulfidic Sea Stimulated by Early Oxidative Weathering of the Continents. Science 326, 713-716.

Rudnick, R.L., Gao, S., 2014. Composition of the Continental Crust. Treatise on Geochemistry (Second Edition) 4, 1-51.

Rudnick, R.L., Tomascak, P.B., Njo, H.B., Gardner, L.R., 2004. Extreme lithium isotopic fractionation during continental weathering revealed in saprolites from South Carolina. Chemical Geology 212, 45-57.

Sahoo, S. K., Planavsky, N. J., Kendall, B., Wang, X., Shi, X., Scott, C., Anbar, A. D., Lyons, T. W. and Jiang, G., 2012. Ocean oxygenation in the wake of the Marinoan glaciation. Nature 489, 546-549.

Sauzéat, L., Rudnick, R.L., Chauvel, C., Garçon, M., Tang, M., 2015. New perspectives on the Li isotopic composition of the upper continental crust and its weathering signature. Earth and Planetary Science Letters 428, 181-192.

Scholz, F., Beil, S., Flögel, S., Lehmann, M. F., Holbourn, A., Wallmann, K. and Kuhnt, W., 2019. Oxygen minimum zone-type biogeochemical cycling in the Cenomanian-Turonian Proto-North Atlantic across Oceanic Anoxic Event 2. Earth and Planetary Science Letters 517, 50-60.

Scott, C., Lyons, T. W., Bekker, A., Shen, Y., Poulton, S. W., Chu, X. and Anbar, A. D., 2008. Tracing the stepwise oxygenation of the Proterozoic ocean. Nature 452, 456-459.

Shields G., Stille P., Brasier M.D. and Atudorei N.V., 1998. Stratified oceans and oxygenation of the late Precambrian environment: a post glacial geochemical record from the Neoproterozoic of W. Mongolia. Terra Nova 9(5-6), 218-222.

Taylor S.R., McLennan S.M., 1985. The Continental Crust: Its Composition and Evolution. Blackwell, Oxford.

Tomascak, P.B., Langmuir, C.H., le Roux, P.J. and Shirey, S.B., 2008. Lithium isotopes in global mid-ocean ridge basalts. Geochimica et Cosmochimica Acta 72, 1626-1637.

Torres, M. A., Moosdorf, N., Hartmann, J., Adkins, J. F. and West, A. J., 2017. Glacial weathering, sulfide oxidation, and global carbon cycle feedbacks. Proc. Natl. Acad. Sci. USA 114, 8716-8721.

Tribovillard, N., Algeo, T. J., Baudin, F. and Riboulleau, A., 2012. Analysis of marine environmental conditions based on molybdenum–uranium covariation—Applications to Mesozoic paleoceanography. Chemical Geology 324-325, 46-58.

Verney-Carron, A., Vigier, N., Millot, R., 2011. Experimental determination of the role of diffusion on Li isotope fractionation during basaltic glass weathering. Geochimica et Cosmochimica Acta 75, 3452-3468.

Wang, J., Li, Z.-X., 2003. History of Neoproterozoic rift basins in South China: implications for Rodinia break-up. Precambrian Research 122, 141-158.

Wei, W., Frei, R., Klaebe, R., Li, D., Wei, G.Y., Ling, H.F., 2018. Redox condition in the Nanhua Basin during the waning of the Sturtian glaciation: A chromium-isotope perspective. Precambrian Research 319, 198-210.

Wei, W., Wang, D., Li, D., Ling, H.-F., Chen, X., Wei, G.-Y., Zhang, F., Zhu, X., Yan, B., 2016.

The marine redox change and nitrogen cycle in the early Cryogenian interglacial time: evidence from nitrogen isotopes and Mo contents of the basal Datangpo Formation, Northeastern Guizhou, South China. Journal of Earth Science 27, 233-241.

Whitfield M., Turner D.R., 1979. Water–rock partition coefficients and the composition of seawater and river water. Nature 278, 132–137.

Wimpenny, J., Colla, C.A., Yu, P., Yin, Q.-Z., Rustad, J.R., Casey, W.H., 2015. Lithium isotope fractionation during uptake by gibbsite. Geochimica et Cosmochimica Acta 168, 133-150.

Wimpenny, J., Gíslason, S.R., James, R.H., Gannoun, A., Pogge Von Strandmann, P.A.E., Burton, K.W., 2010a. The behaviour of Li and Mg isotopes during primary phase dissolution and secondary mineral formation in basalt. Geochimica et Cosmochimica Acta 74, 5259-5279.

Wimpenny, J., James, R.H., Burton, K.W., Gannoun, A., Mokadem, F., Gíslason, S.R., 2010b. Glacial effects on weathering processes: New insights from the elemental and lithium isotopic composition of West Greenland rivers. Earth and Planetary Science Letters 290, 427-437.

Weaver, C.E., 1989. Clays, muds, and shales (Developments in Sedimentology). Elsevier, New York.

Zhang, F., Zhu, X., Yan, B., Kendall, B., Peng, X., Li, J., Algeo, T.J., Romaniello, S., 2015. Oxygenation of a Cryogenian ocean (Nanhua Basin, South China) revealed by pyrite Fe isotope compositions. Earth and Planetary Science Letters 429, 11-19.

Zhang, Q., Chu, X., Bahlburg, H., Feng, L., Dobrzinski, N., Zhang, T., 2003. Stratigraphic architecture of the Neoproterozoic glacial rocks in the “Xiang-Qian-Gui” region of the central Yangtze Block, South China. Progress in Natural Science 13, 783-787.

Zhang, S., Jiang, G., Han, Y., 2008. The age of the Nantuo Formation and Nantuo glaciation in South China. Terra Nova 20, 289-294.

Zhou, C., Huyskens, M.H., Lang, X., Xiao, S., Yin, Q.-Z., 2019. Calibrating the terminations of Cryogenian global glaciations. Geology 47, 251-254.

Figure captions

Figure 1. Paleogeographic map of South China in the Cryogenian deglaciation and lithostratigraphy of the Cryogenian succession in the studied Daotuo section. Radiometric dating for Datangpo Formation is on basis of Zhou et al. (2019) for the basal Datangpo Formation and Zhang et al. (2008) for the uppermost Datangpo Formation.

Figure 2. Profiles of δ^7Li, Total organic carbon (TOC), Li concentration, Li/Al ratio and Al/Si ratio of the Datangpo Formation in the Daotuo section. The shaded area in (A) represents the range of δ^7Li values for the upper continental crust (UCC) (Sauzéat et al., 2015). The dashed line in (E) represents the threshold for coarse–fine grain (Bouchez et al., 2011; Dellinger et al., 2014).

Figure 3. Profiles of Mo concentration, U concentration, Fe/Al ratio and Fe speciation data (Fe_{HR} is highly reactive Fe; Fe_{Py} is Fe in pyrite; Fe_T is total Fe) of the Datangpo Formation in the Daotuo section. The thresholds of Fe speciation analyses in (C), (D) and (E) are modified from Raiswell et al. (2018).

Figure 4. Cross-plots of (A) Be vs. Al, (B) Sc vs. Al, (C) Ti vs. Al, and (D) Th vs. Al of the bulk samples in the Daotuo section. R^2 represents the coefficient of determination of the correlations. The average ratios of Al/Be, Al/Sc, Al/Ti and Al/Th for the studied samples and

the UCC (data from Rudnick and Gao, 2014) are shown in each figure.

Figure 5. Cross-plots of (A) δ^7Li vs. Al/Si ratio and (B) Na/Al ratio vs. Li/Al ratio for the bulk samples in the Daotuo section. The dashed curve in (A) represents δ^7Li values of modern river sediments as a function of Al/Si ratio (modified after Dellinger et al., 2014), used as a proxy for detrital grain size. Low Al/Si ratio (< 0.15) are modified from river bed sands and high Al/Si ratio are modified from finely ground suspended sediments. The dashed arrow in (B) represents the mixing line of igneous rock debris and sedimentary rock debris (modified after Dellinger et al., 2014).

Figure 6. Cross-plots of (A) δ^7Li vs. Li concentration and (B) δ^7Li vs. Li/Al ratio for the bulk samples in the Daotuo section. The dashed lines are the results of two endmember mixture for δ^7Li values of bulk samples in this study. R^2 represents the coefficient of determination of the correlations. Endmember A represents physical eroded mafic rock with high δ^7Li and low Li concentration (δ^7Li ≈ 6.18‰, [Li] ≈ 11.80 ppm, Li/Al ≈ 1.95); endmember B represents highly-congruent weathering product with low δ^7Li and relatively low Li concentration (δ^7Li ≈ -4.98‰, [Li] ≈ 36.96 ppm, Li/Al ≈ 3.46); and endmember C represents incongruent weathering product with relatively high δ^7Li and Li concentration (δ^7Li ≈ -1.53‰, [Li] ≈ 62.93 ppm, Li/Al ≈ 7.00) (above data are modified from Pogge von Strandmann et al., 2006, 2010; Wimpenny et al., 2010b; Millot et al., 2010; Dellinger et al., 2014; 2017 and references therein).

Figure 7. Cross plots of (A) Fe_T vs. Al concentration, (B) Fe_{Py}/F_{HR} vs. Fe_{HR}/Fe_T, (C) Mo vs. TOC concentration and (D) Mo_{EF} vs. U_{EF} for the studied samples in the Daotuo section. In (A), Fe_T of all studied samples are higher than 0.5%. In (B), the boundaries between oxic and anoxic conditions (Fe_{HR}/Fe_T = 0.22–0.38) and between ferruginous-anoxic and euxinic-anoxic

condition (Fe_{Py}/Fe_{HR} = 0.7–0.8) are on basis of Raiswell et al. (2018). In (C), Mo vs. TOC diagrams of modern marine sediments are modified from Algeo et al. (2006). The slopes of each line are 45 ± 5 (Saanich Inlet), 25 ± 5 (Cariaco Basin), 9 ± 2 (Framvaren Fjord) and 4.5 ± 1 (Black Sea), respectively, which represent the Mo–TOC correlations of the marine sediments in various modern anoxic depositional environment. In (D), the curves represent the co-varying Mo_{EF} and U_{EF} of the marine sediments in different modern depositional environment (i.e., open marine setting, Cariaco Basin and Black Sea) (Algeo and Tribovillard, 2009).

Figure 8. Co-variations between δ^7Li and Fe_{HR}/Fe_T, Fe_{Py}/Fe_{HR} for the studied samples in the Daotuo section. The boundaries between oxic and anoxic conditions (Fe_{HR}/Fe_T = 0.22–0.38) and between ferruginous-anoxic and euxinic-anoxic condition (Fe_{Py}/Fe_{HR} = 0.7–0.8) are on basis of Raiswell et al. (2018). The arrows represent the systematic tendency for extensive marine anoxia and euxinia following the increase in silicate weathering intensity.

Figure 9. Schematic diagram of links between continental weathering and marine redox states over continental margin during the Cryogenian non-glacial interval. (A) Stage A, high physical erosion dominated post-glaciation, low primary production and no euxinic seawater on the continental margin; (B) Stage B, congruent chemical weathering (high silicate weathering intensity and flux) in the early interglacial period, high primary production and expanded euxinic seawater on the continental margin; (C) Stage C, incongruent chemical weathering (moderate silicate weathering intensity and low weathering flux) in the middle and late non-glacial interval, low primary production and diminished euxinic seawater on the continental margin.

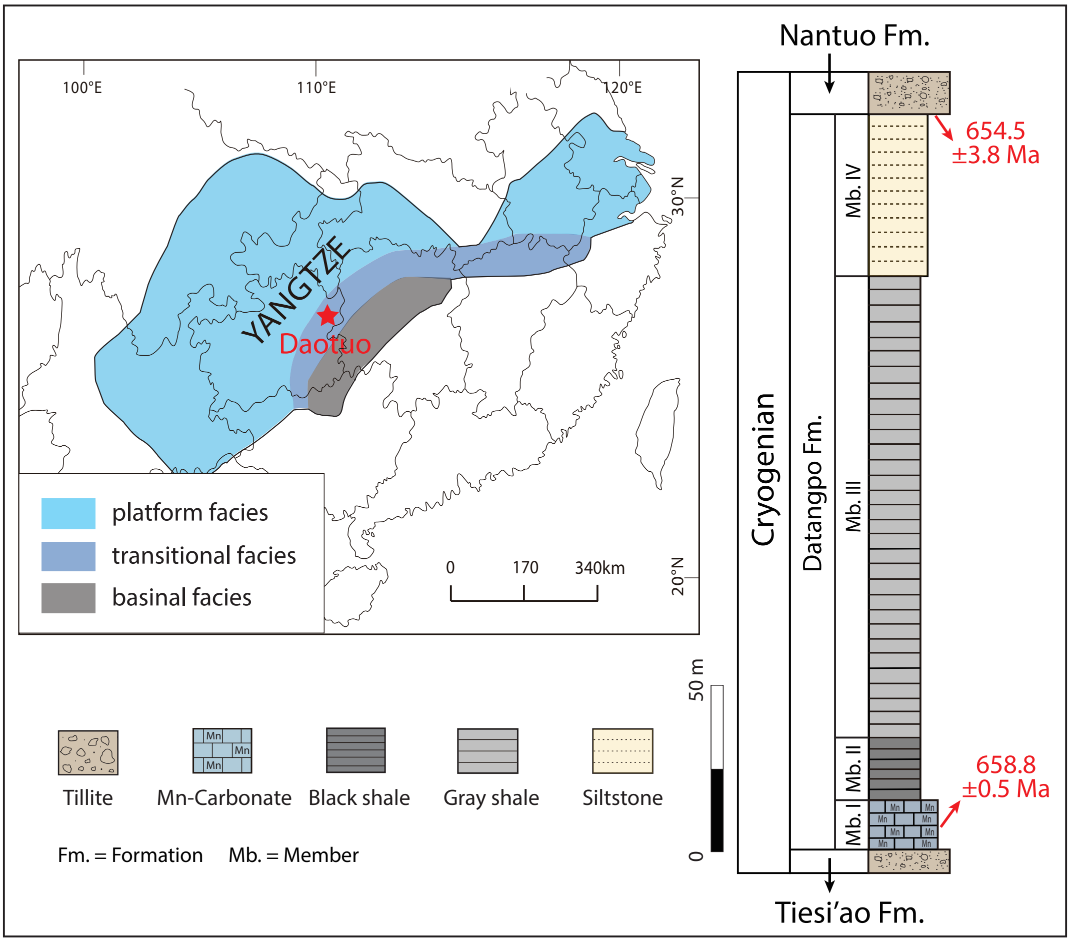
100°E
110°E
120°E
30°N
20°N
YANGTZE
Daotuo
platform facies
transitional facies
basinal facies
0
170
340km
Tillite
Mn-Carbonate
Black shale
Gray shale
Siltstone
Fm. = Formation
Mb. = Member
50 m
0
Nantuo Fm.
Cryogenian
Datangpo Fm.
Mb. IV
Mb. III
Mb. II
Mb. I
654.5
±3.8 Ma
658.8
±0.5 Ma
Tiesi'ao Fm.

Figure 1

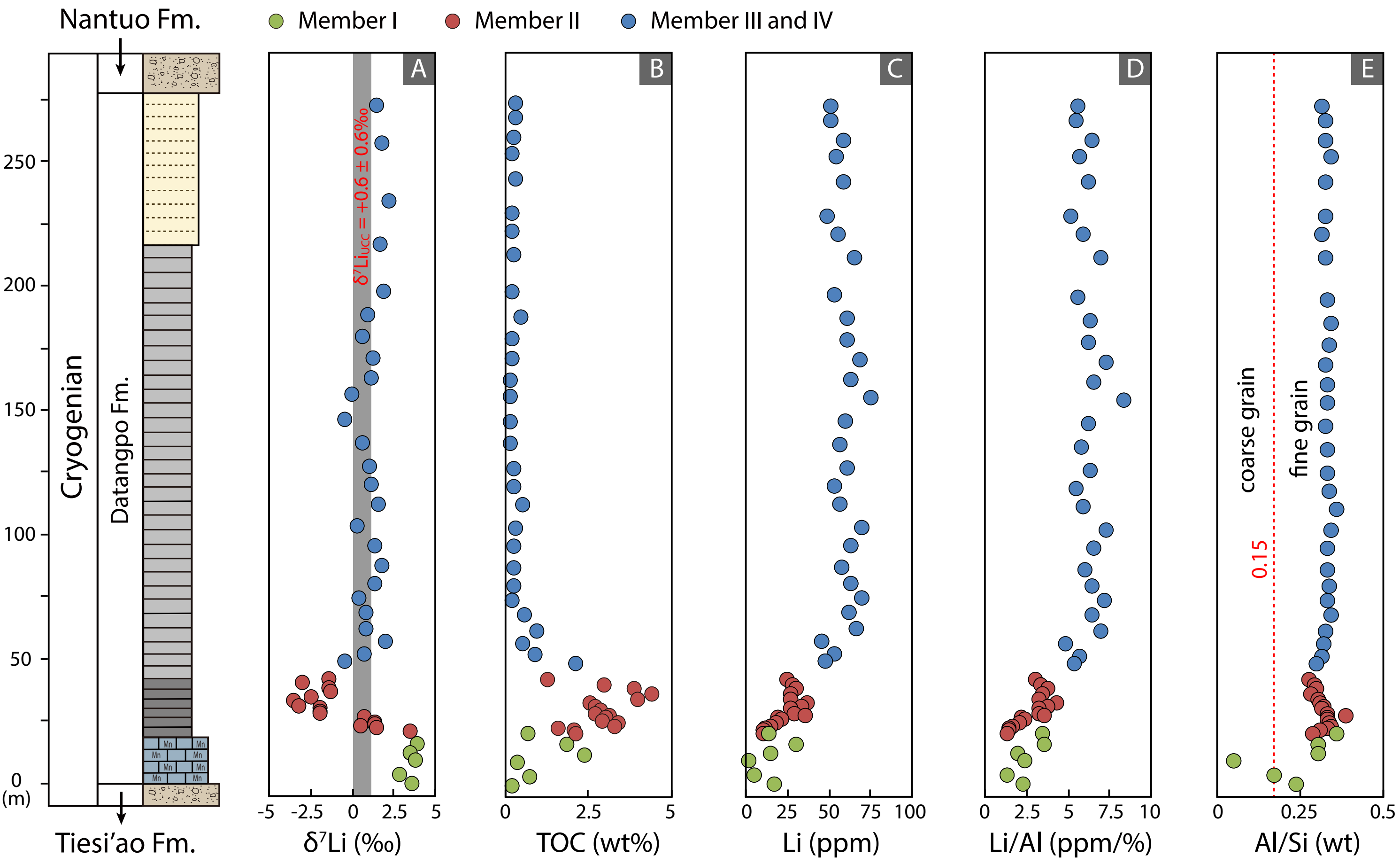
Nantuo Fm.
Member I
Member II
Member III and IV
A
B
C
D
E
Cryogenian
Datangpo Fm.
250
200
150
100
50
0
(m)
Mn
Tiesi'ao Fm.
δ7LiUCC = +0.6 ± 0.6‰
coarse grain
fine grain
0.15
-5
-2.5
0
2.5
5
δ7Li (‰)
0
2.5
5
TOC (wt%)
0
25
50
75
100
Li (ppm)
0
2.5
5
7.5
10
Li/Al (ppm/%)
0
0.25
0.5
Al/Si (wt)

Figure 2

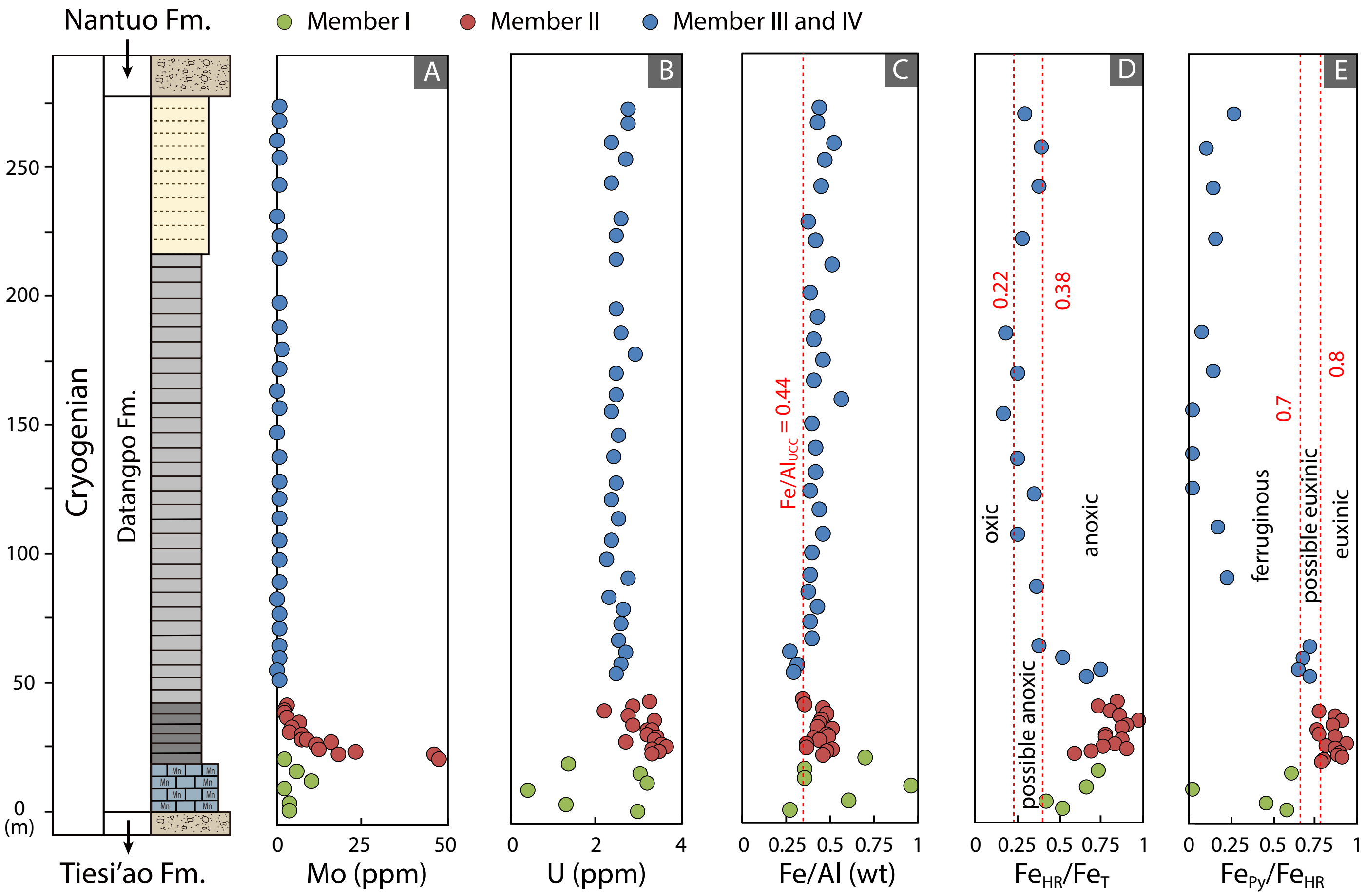
Nantuo Fm.
Member I
Member II
Member III and IV
Cryogenian
Datangpo Fm.
Mn
250
200
150
100
50
0
(m)
Tiesi'ao Fm.
A
0
25
50
Mo (ppm)
B
0
2
4
U (ppm)
C
Fe/Al$_{UCC}$ = 0.44
0
0.25
0.5
0.75
1
Fe/Al (wt)
D
0.22
0.38
oxic
possible anoxic
anoxic
0
0.25
0.5
0.75
1
Fe$_{HR}$/Fe$_T$
E
0.7
0.8
ferruginous
possible euxinic
euxinic
0
0.25
0.5
0.75
1
Fe$_{Py}$/Fe$_{HR}$

Figure 3

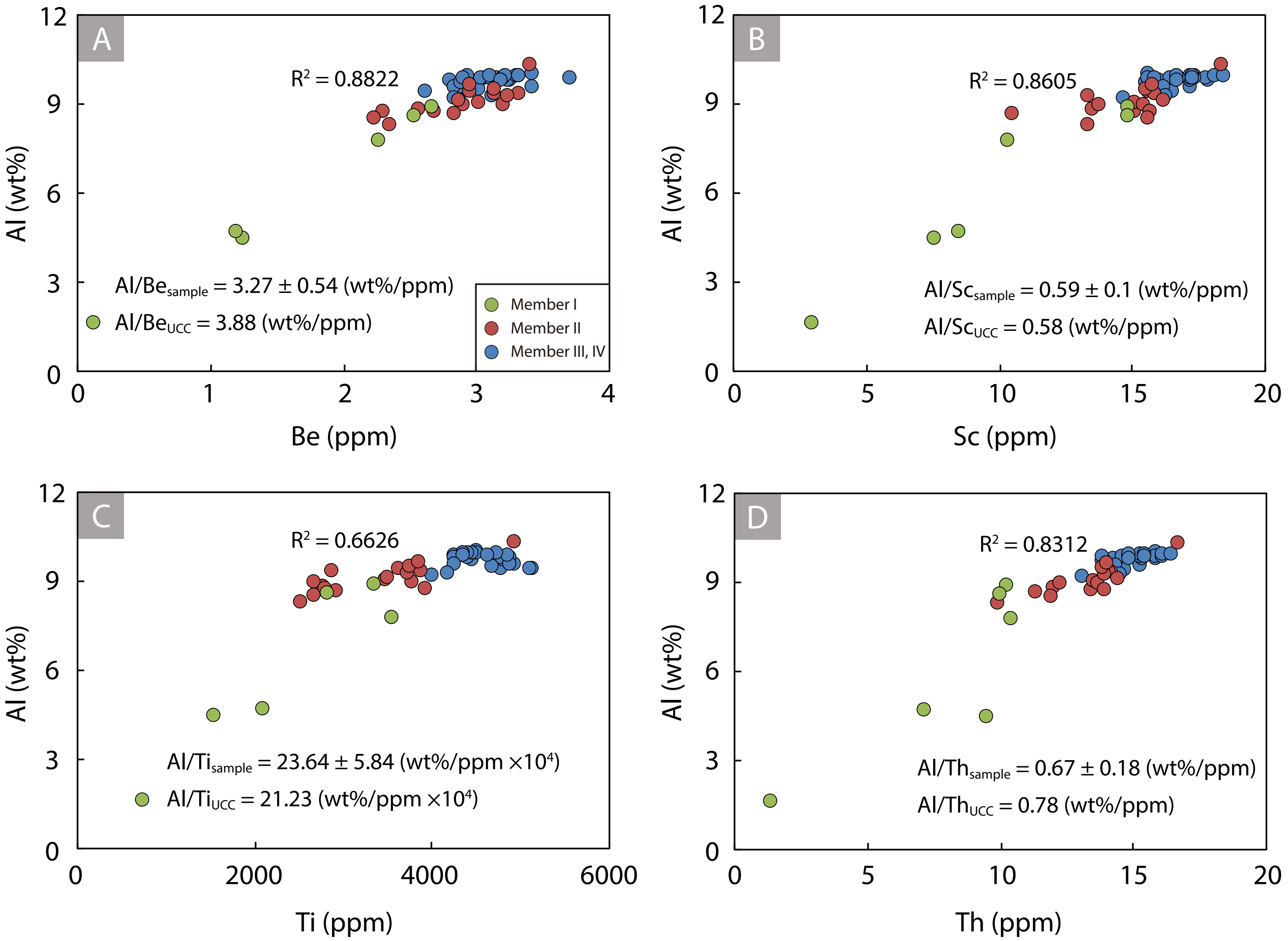
A
R² = 0.8822
Al/Be_sample = 3.27 ± 0.54 (wt%/ppm)
Al/Be_UCC = 3.88 (wt%/ppm)
Member I
Member II
Member III, IV
Al (wt%)
Be (ppm)
0
3
6
9
12
0
1
2
3
4
B
R² = 0.8605
Al/Sc_sample = 0.59 ± 0.1 (wt%/ppm)
Al/Sc_UCC = 0.58 (wt%/ppm)
Al (wt%)
Sc (ppm)
0
5
10
15
20
C
R² = 0.6626
Al/Ti_sample = 23.64 ± 5.84 (wt%/ppm ×10⁴)
Al/Ti_UCC = 21.23 (wt%/ppm ×10⁴)
Al (wt%)
Ti (ppm)
0
2000
4000
6000
D
R² = 0.8312
Al/Th_sample = 0.67 ± 0.18 (wt%/ppm)
Al/Th_UCC = 0.78 (wt%/ppm)
Al (wt%)
Th (ppm)

Figure 4

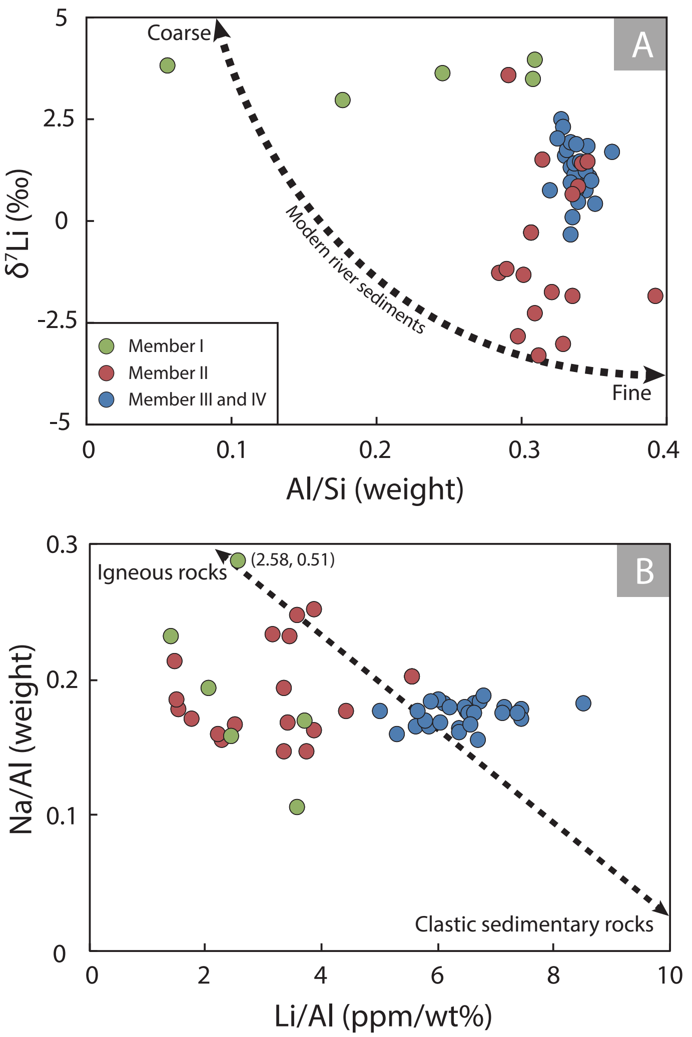
A
Coarse
Fine
Modern river sediments
Member I
Member II
Member III and IV
δ7Li (‰)
5
2.5
0
-2.5
-5
0
0.1
0.2
0.3
0.4
Al/Si (weight)
B
Igneous rocks
(2.58, 0.51)
Clastic sedimentary rocks
Na/Al (weight)
0.3
0.2
0.1
0
0
2
4
6
8
10
Li/Al (ppm/wt%)

Figure 5

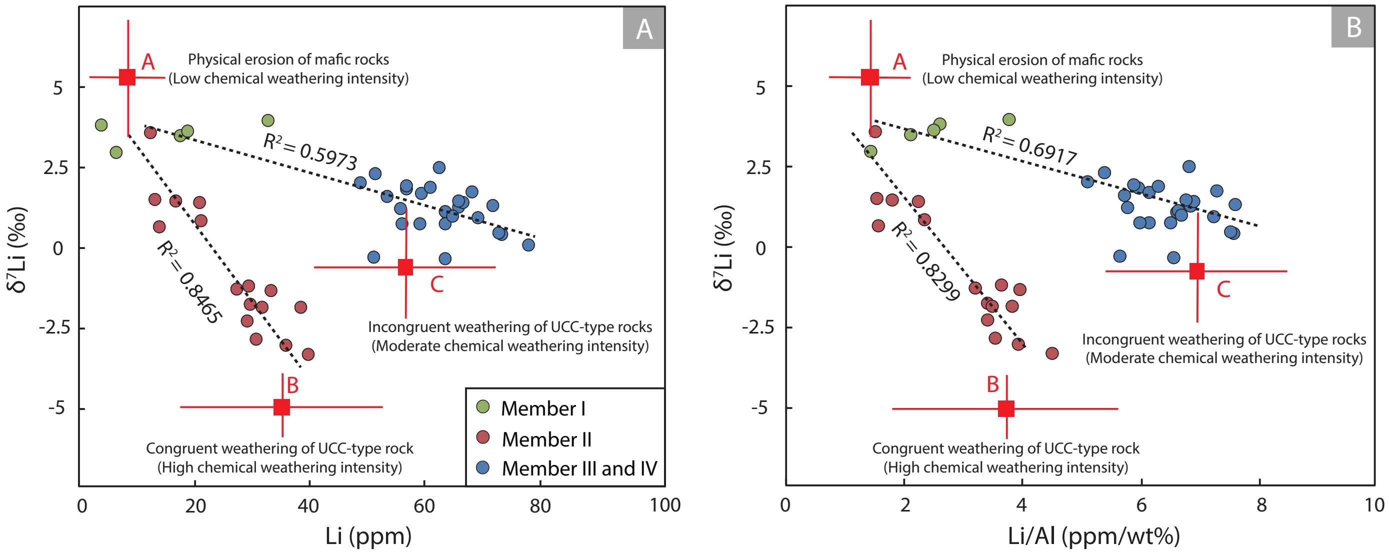
A
Physical erosion of mafic rocks
(Low chemical weathering intensity)
$R^2 = 0.5973$
$R^2 = 0.8465$
B
C
Incongruent weathering of UCC-type rocks
(Moderate chemical weathering intensity)
Congruent weathering of UCC-type rock
(High chemical weathering intensity)
● Member I
● Member II
● Member III and IV
δ7Li (‰)
5
2.5
0
-2.5
-5
0
20
40
60
80
100
Li (ppm)
B
$R^2 = 0.6917$
$R^2 = 0.8299$
0
2
4
6
8
10
Li/Al (ppm/wt%)

Figure 6

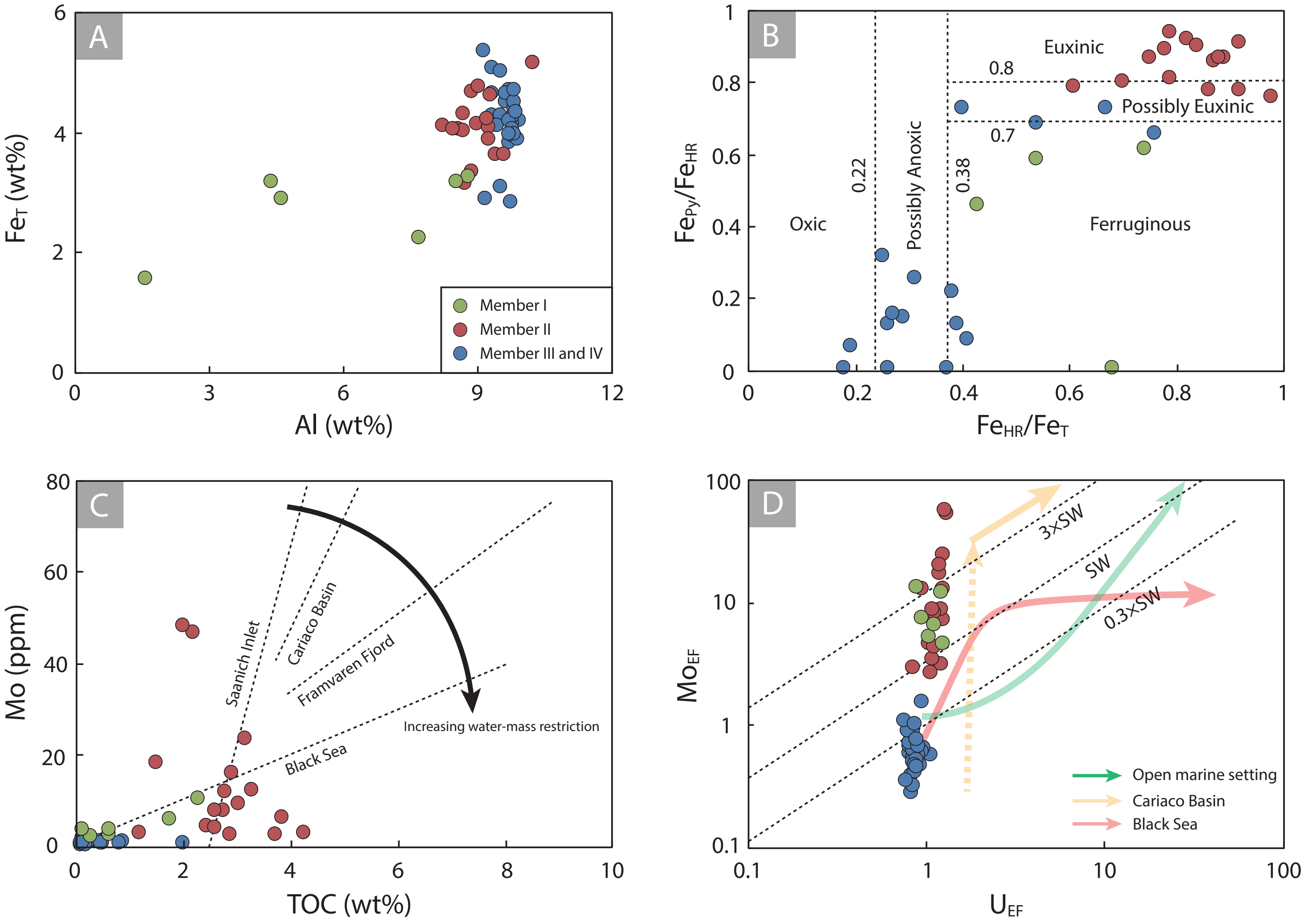
A
Fe$_T$ (wt%)
Al (wt%)
0
2
4
6
0
3
6
9
12
Member I
Member II
Member III and IV
B
Fe$_{Py}$/Fe$_{HR}$
Fe$_{HR}$/Fe$_T$
0
0.2
0.4
0.6
0.8
1
Oxic
0.22
Possibly Anoxic
0.38
Euxinic
0.8
Possibly Euxinic
0.7
Ferruginous
C
Mo (ppm)
TOC (wt%)
0
20
40
60
80
0
2
4
6
8
10
Saanich Inlet
Cariaco Basin
Framvaren Fjord
Black Sea
Increasing water-mass restriction
D
Mo$_{EF}$
U$_{EF}$
0.1
1
10
100
3×SW
SW
0.3×SW
Open marine setting
Cariaco Basin
Black Sea

Figure 7

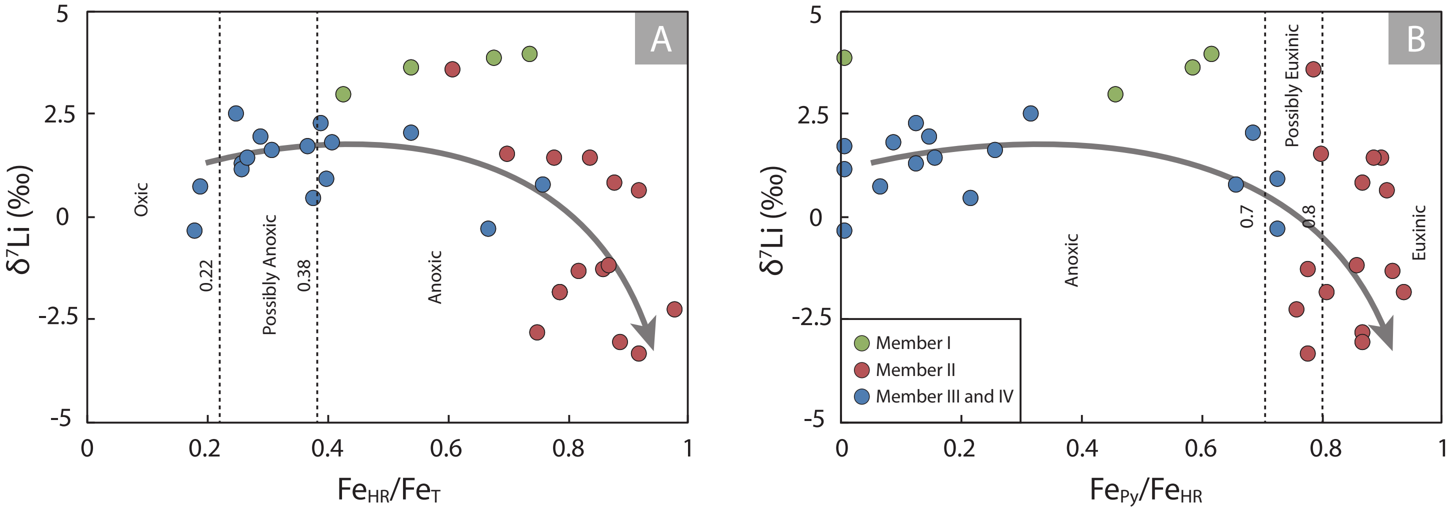
A
δ7Li (‰)
5
2.5
0
-2.5
-5
0
0.2
0.4
0.6
0.8
1
FeHR/FeT
Oxic
0.22
Possibly Anoxic
0.38
Anoxic
B
FePy/FeHR
Anoxic
0.7
0.8
Possibly Euxinic
Euxinic
● Member I
● Member II
● Member III and IV

Figure 8

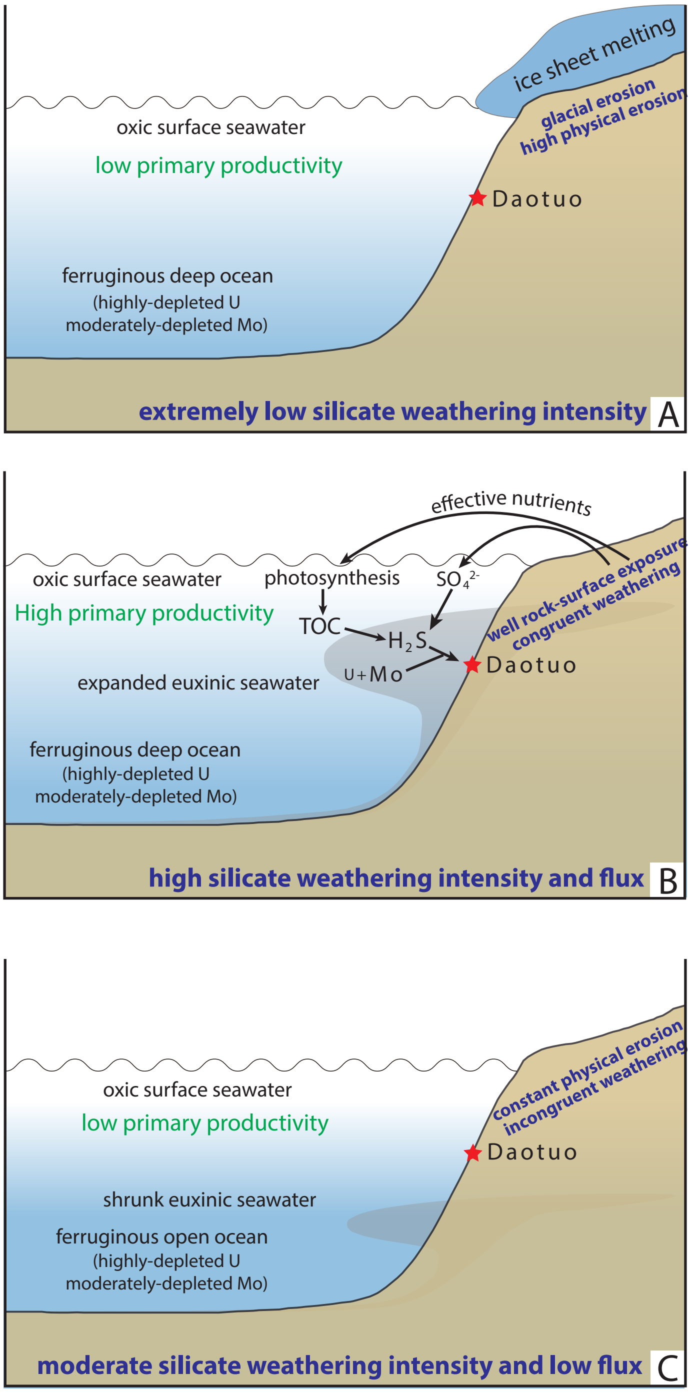
ice sheet melting
glacial erosion
high physical erosion
oxic surface seawater
low primary productivity
Daotuo
ferruginous deep ocean
(highly-depleted U
moderately-depleted Mo)
extremely low silicate weathering intensity
A
effective nutrients
oxic surface seawater
photosynthesis
SO_4^{2-}
High primary productivity
TOC
H_2S
well rock-surface exposure
congruent weathering
Daotuo
U+Mo
expanded euxinic seawater
ferruginous deep ocean
(highly-depleted U
moderately-depleted Mo)
high silicate weathering intensity and flux
B
oxic surface seawater
low primary productivity
constant physical erosion
incongruent weathering
Daotuo
shrunk euxinic seawater
ferruginous open ocean
(highly-depleted U
moderately-depleted Mo)
moderate silicate weathering intensity and low flux
C

Figure 9